energies

MDPI

Review

The Application of Crystallization Kinetics in Optimizing Morphology of Active Layer in Non-Fullerene Solar Cells

Longjing Wan [1,2], Wangbo Wu [2], Ming Jiang [2], Xipeng Yin [2], Zemin He [1,2,*] and Jiangang Liu [1,2,*]

[1] Xi'an Key Laboratory of Advanced Photo-Electronics Materials and Energy Conversion Device, School of Electronic Information, Xijing University, Xi'an 710123, China
[2] School of Electronics and Information, Northwestern Polytechnical University, Xi'an 710129, China; yinxipeng@nwpu.edu.cn (X.Y.)
* Correspondence: 20180083@xijing.edu.cn (Z.H.); jgliu@nwpu.edu.cn (J.L.)

Abstract: Organic photovoltaics (OPVs) have attracted widespread attention and became an important member of clean energy. Recently, their power conversion efficiency (PCE) has surpassed 19%. As is well known, the morphology of the active layer in OPVs crucially influences the PCE. In consideration of the intricate interactions between the donor molecules and acceptor molecules, the precise control of the morphology of the active layer is extremely challenging. Hence, it is urgent to develop effective methods to fabricate the hierarchical structure of the active layer. One significant driving force for the morphological evolution of the active layer is crystallization. Therefore, regulating the crystallization kinetics is an effective strategy for morphology control. In this review, we present the kinetic strategies recently developed to highlight their significance and effectiveness in morphology control. By applying these kinetic strategies, the hierarchical structure, including phase separation, domain size, crystallinity, and molecular orientation of the active layer can be optimized in different blend systems, leading to an improved PCE of OPVs. The outcomes set the stage for future advancements in device performance.

Keywords: organic solar cells; diffusivity; film-forming process; crystallization; morphology; kinetics

check for updates

Citation: Wan, L.; Wu, W.; Jiang, M.; Yin, X.; He, Z.; Liu, J. The Application of Crystallization Kinetics in Optimizing Morphology of Active Layer in Non-Fullerene Solar Cells. *Energies* **2024**, *17*, 2262. https://doi.org/10.3390/en17102262

Academic Editor: Luigi Vesce

Received: 31 March 2024
Revised: 23 April 2024
Accepted: 2 May 2024
Published: 8 May 2024

Copyright: © 2024 by the authors. Licensee MDPI, Basel, Switzerland. This article is an open access article distributed under the terms and conditions of the Creative Commons Attribution (CC BY) license (https://creativecommons.org/licenses/by/4.0/).

1. Introduction

Organic photovoltaics (OPVs), that convert solar energy into electric energy, offer a wide range of potential applications because of their special benefits, including low cost, flexibility, and simplicity in large-scale solution preparation [1–7]. With the help of molecular synthesis [8–10], and device engineering [11–13] and morphology control [14–19], OPVs' power conversion efficiency (PCE) with bulk heterojunction (BHJ) structures has surpassed 19% [20–23]. Nonetheless, OPVs' PCE still lags behind that of silicon- or perovskite-based solar cells [24,25]. Thus, it is imperative and significant to improve the PCE further for both industry and academic research on OPVs [26,27].

The structure of an OPV is shown in Figure 1A,B [28]. Take the inverted device as an example, an OPV normally includes five components, including a glass substrate with an electrode, a hole transport layer (cathode interface layer), an active layer, an electron layer (anode interface layer), and an electrode. As shown in Figure 1C, the photoelectric conversion processes of OPVs mainly include five steps: photon absorption, the diffusion and dissociation of excitons, carrier transport, and collection [2,29–31]. Numerous studies have shown that the active layer's morphology plays a major role in controlling how well an OPV device performs [32–34]. According to recent research, proper mixing of the donor and acceptor in the active layer is necessary to ensure that the photoelectric conversion process proceeds without hiccups [35–37]. In particular, it is necessary to form a crystalline interpenetrating network with domain size of 10–20 nm to ensure excitons diffuse to the D/A interface during the lifetime [38–40]. Additionally, to promote the vertical carrier transport at the donor–acceptor interface, the donor and acceptor must adopt the same

molecular orientation [41–44]. When the donor and acceptor molecules have the same orientation, the interface between them will be more organized, which will help to form a continuous charge separation interface at the interface, reduce charge recombination, and improve the photoelectric conversion efficiency [45,46]. Furthermore, adequate crystallinity and domain purity are crucial for carrier transport [47–49]. Excessive crystallinity leads to an increase in crystal defects, which reduces the charge mobility and at the same time decreases the light absorption capacity of the active layer; too low a crystallinity leads to the presence of amorphous-oriented and unneeded structures in the active layer, which affects the charge transport. High domain purity leads to serious phase separation in the D/A interface and low exciton diffusion efficiency, while low domain purity leads to bimolecular recombination in the process of carrier transport. Meanwhile, film roughness is directly related to the degree of molecular crystallinity. Suitable roughness increases in the boundary area, which improves the separation efficiency of electrons and holes and facilitates charge transport within the active layer [50,51]. In addition, an appropriate vertical phase separation must be formed in accordance with the device structure [52,53]. When a phase-separated structure is formed in which the donor and acceptor materials are enriched in the vicinity of the anode and cathode, respectively, the compounding of electrons and holes in the transport process can be reduced, and carrier transport and collection can be minimized. However, such ideal morphology is difficult to obtain due to the intricate interaction between the donor and acceptor [54–56].

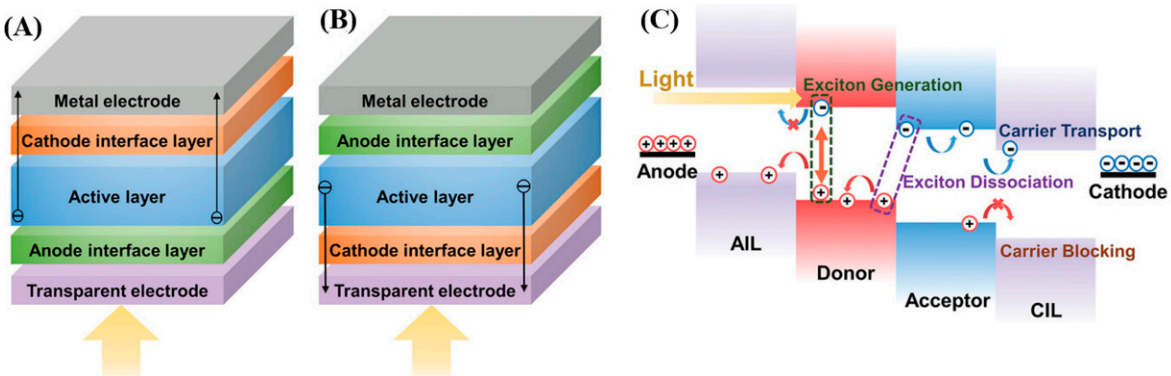

Figure 1. The structure of single-junction OPVs and working mechanism illustration. OPV devices in (**A**) conventional structure or (**B**) inverted structure. (**C**) The working mechanism of carrier generation and transport in OPVs. Reproduced with permission from [28], WILEY-VCH, 2023.

In the last decade, numerous techniques have been explored for improving the active layer's morphology. Currently, thermal annealing (TA) [57–60], solvent vapor annealing (SVA) [61–63], controlling the solution state [64,65], and adding additives [66–68] are the primary worldwide approaches. Even though these techniques are successfully applied in optimizing the active layer's morphology, they invariably run into a number of difficulties in fabricating a nanoscale crystalline interpenetrating network due to the rigidity of conjugated molecules as well as the coupling of crystallization between the donor and acceptor [69,70]. Specifically speaking, the working mechanism has not been investigated thoroughly, especially from the viewpoint of the film evolution process and crystallization kinetics [71–74]. The reasons for this include, but are not limited to, the following: (1) in non-fullerene solar cells, the intricate interactions between the donor and acceptor molecules are very complicated, including intermolecular stacking, twisting, and aggregation, thus leading to different crystallization kinetics and inaccurate correlation between crystallization kinetics and molecular features in diversified systems [75]; (2) the multiphase mixing domain of donor–acceptor–additives during the solution-to-film process gives rise to a variety of possibilities of interactions, crystallization, and phase-separation behaviors, which makes it ambiguous to establish the relationship between different crystallization kinetics and the morphology of the active layer [70]; (3) in the process of solution

processing, the time of molecular transformation from the amorphous state in solution to the aggregation state in the film is very short, even less than 1 s in CF solvent, so it is difficult to monitor the crystallization behavior of molecules in the film formation process, including nucleation, crystal growth, and crystallization rate [66]; and (4) in some systems, the intrinsic properties of the donor and acceptor are similar, so it is difficult to distinguish the difference of crystallization kinetics between the donor and acceptor [76].

In morphology optimization and device performance improvement, charge transport layers also play a critical role. Due to the robust coulombic interactions between electrons and holes in OPVs, both geminate and non-geminate recombination occur during the processes of charge separation and transport [77]. These phenomena contribute significantly to the decrease in PCE. An efficient charge transport layer can passivate interface defects and increase OPVs' PCE and stability [34,78]. The charge transport layers can influence the film morphology, in that through the interface, the surface energy can be significantly tuned to facilitate the formation of a bicontinuous network in the active layer and induce proper crystallized domains [79]. In addition, the charge transport layer can influence the preferred orientation of the active-layer materials, resulting in morphology control [80,81].

Aiming at solving the above problems, an effective strategy is developed via regulating the crystallization kinetics of blends [55,82]. The results show that the phase-separated structure, domain size, crystallinity, and molecular orientation of the active layer can be optimized through regulating the diffusivity, the relative rate of nucleation and crystal growth, and the sequence of crystallization of the donor and acceptor [83–85]. The optimized morphology is beneficial to device performance, including suppressing exciton quenching, recombination of the charge-transfer state (CT state), bimolecular recombination, and improving charge mobility, which lays a solid foundation for OPVs with high performance. The following sections will detail the methods of regulating the film-formation kinetics to optimize the active layer morphology and enhance device performance.

2. Influence of Crystallization Kinetics on Morphology of Active Layer

Film-forming kinetics pertains to the scientific principles and dynamic mechanisms governing the deposition and development of the film morphology of OPVs, in which crystallization kinetics plays a pivotal role in influencing the phase separation process to form the final morphology. In the initial stage of film forming, the molecular clusters begin to nucleate, and then, grow and form aggregates. When the solution reaches the solubility limit, the molecules begins to crystallize, accompanied by liquid–liquid separation and solid–liquid separation [86].

It is proposed that the construction principle of a highly crystalline bicontinuous network structure is as follows: if the polymer's donor formation network has a weak restriction on the small-molecule acceptor, the donor molecule should crystallize before the acceptor molecule, and the molecules crystallized after precipitation should fill into the donor molecule's network, and ultimately the interpenetrating network structure will be formed. If the polymer's donor formation network is more restrictive to the small-molecule acceptor, the small-molecule acceptor should be promoted to crystallize first to reduce the restriction of the polymer's donor crystallization network on the diffusion and aggregation of small molecules, to improve the crystallinity of the small-molecule acceptor, and ultimately to form a highly crystalline interpenetrating network structure. For example, Chen et al. proposed accelerating the aggregation rate of the acceptor L8-BO in the D18-Fu:L8-BO system using the solid additive 2-CN, which contributes to the formation of the acceptor phase with a higher crystallinity, and thus, forms an ideal bicontinuous network structure. The addition of 2-CN accelerated the time of the solution removal and thin-film-thinning phases, stabilized the peak fluctuation of the donor during the solution removal phase, and achieved a more controllable donor aggregation behavior [87]. Therefore, optimizing the morphology of the active layer by regulating the crystallization kinetics behavior is very effective, and this technology is also compatible with large-area solution processing of organic photovoltaic cells, and has great potential.

Here, we list in Table 1 related regulation methods of crystallization kinetics that are discussed in the following sections, in order to provide a comprehensive overview of this review.

3. Regulating Film-Forming Process to Fabricate Highly Crystalline Interpenetrating Network

3.1. Fabricating Bicontinuous Structure via Film-Forming Kinetics

The charge transmission and collection in OPVs are mostly determined by the interpenetrating network. The ratio and miscibility between the donor molecules and acceptor molecules must be carefully chosen to build bicontinuous networks. It is found that the ratio which is close to the hypoeutectic point is of benefit for fabricating bicontinuous networks [49,88]. However, in some polymer/non-fullerene blends, the continuous pathway cannot be formed even though the ratio is near the hypoeutectic point due to the large difference in crystallization behavior between the donor and acceptor. Therefore, how to regulate the crystallization behavior of the active layer to promote the formation of the bicontinuous phase is particularly important.

The kinetics in the film-forming process has profound impacts on phase separation in the active layer [89,90], including consequences on the crystallization of the donor and acceptor and on the film-forming duration. Liang et al. finely regulated the film-forming process of P3HT:O-IDTBR through adding 1,2,4-triclorobenzene (TCB) into chlorobenzene (CB) solution, and revealed the effect of crystallization on phase separation [91].

P3HT and O-IDTBR stay well dissolved throughout stage I. During stage II, P3HT and O-IDTBR reach their CB solubility limits nearly simultaneously as the solvent keeps evaporating, and the crystallization process ensues. At this point, P3HT and O-IDTBR precipitate concurrently, which seriously interferes with P3HT and O-IDTBR's crystallization process. In stage III, no more P3HT or O-IDTBR crystallites form or grow because the solvent has fully volatilized, greatly suppressing solute movements and ending the crystallization process. The blend system with TCB likewise goes through three stages in the film-forming process (Figure 2C,D). In stages I and III, the film-forming kinetics exhibits a similar tendency to the blend system without TCB. At stage II, however, a great deal of alteration is observed. P3HT initiates nucleation and growth during the early part of stage II (approximately 40–50 s) as a result of CB evaporating. The residual TCB continues to serve as a plasticizer for the P3HT phase during the late stage II (about 60–210 s), allowing for a longer time frame for the organization of P3HT chains. O-IDTBR's aggregating behavior differs from P3HT's in stage II. Only a minor fraction of O-IDTBR aggregates and forms a crystal nucleus during the early part of stage II (35–50 s), with the majority still dispersing in the solvent due to its high solubility in TCB (124 mg mL^{-1}). As TCB evaporates, O-IDTBR begins to crystallize as its concentration exceeds the corresponding saturated solubility in TCB.

Phase separation is significantly impacted by the kinetics of film formation. It is well known that liquid–solid (L-S) or liquid–liquid (L-L) phase separation usually takes place prior to the solvent fully evaporating [92–95]. In the P3HT:O-IDTBR blend without TCB, the donor and acceptor tend to precipitate simultaneously, causing continuous fluctuations in composition. As a result, L-L phase separation occurs, and both P3HT and O-IDTBR crystallize at the same time. In this situation, O-IDTBR molecules disperse in P3HT chains as a result, disrupting the orderly aggregation of both P3HT chains and O-IDTRB. This causes the blends to be quenched into a mixed state, with the coexistence of spherical and fibrous structures, as shown in Figure 2E,F. After the addition of TCB, L-S phase separation is caused by the aggregation of P3HT before O-IDTBR. During this process, P3HT and O-IDTBR crystallize at distinct times, which tends to produce relatively pure phases and can lessen their mutual interference. Thus, crystalline networks of P3HT with nanoscale are formed, which aids the construction of a bicontinous structure with excellent phase purity, as shown in Figure 2G,H.

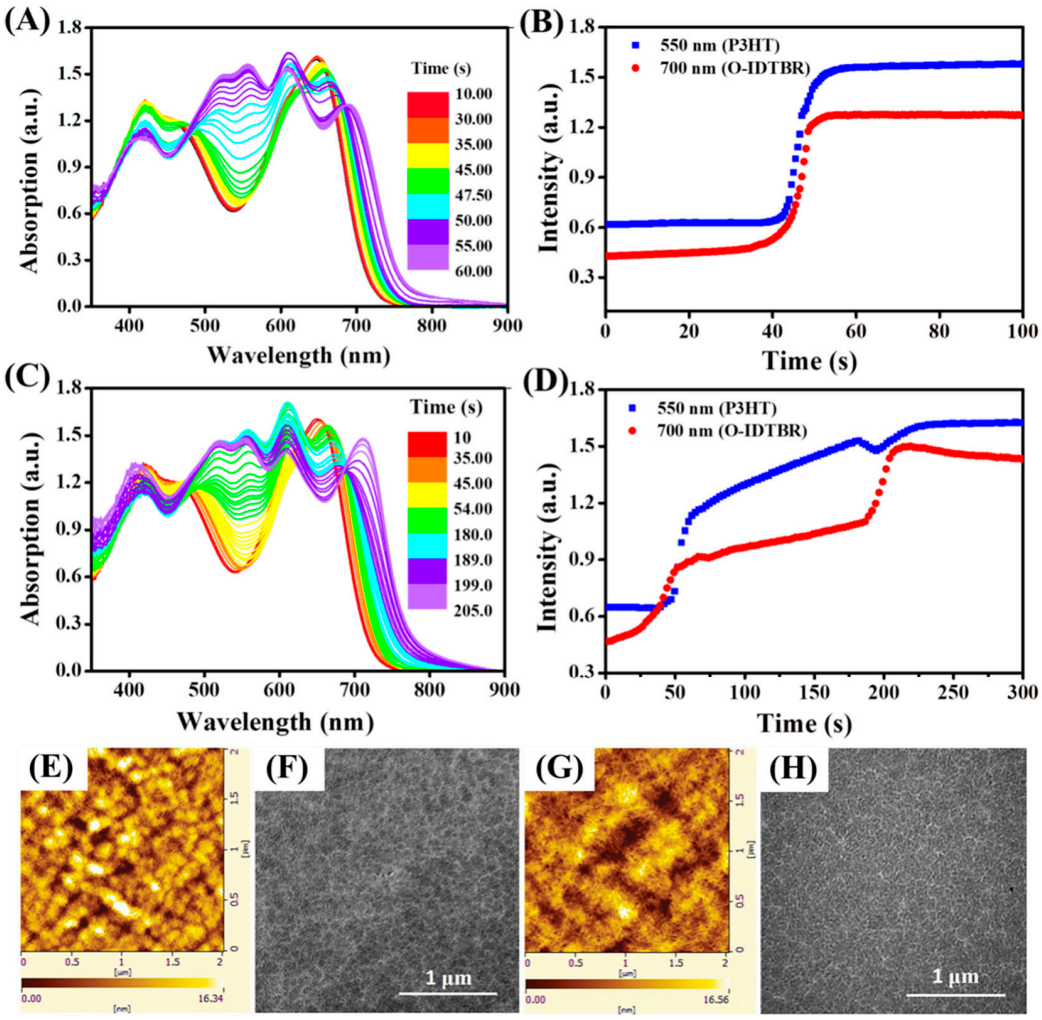

Figure 2. The UV–vis absorption spectra and the evolution of absorption intensity at 550 and 700 nm during film-drying processing without TCB (**A**,**B**) and with TCB (**C**,**D**). The AFM and TEM images for the films without TCB (**E**,**F**) and with TCB (**G**,**H**). Reproduced with permission from [91], WILEY-VCH, 2019.

Charge transport benefits from the active layer's improved phase-separation structure. For the device without TCB, the charge carrier collection probability (P_{coll}) is 83.4%, while it increases to 90.5% for the device with TCB. Furthermore, TCB also contributes to an increase in both hole mobility (μ_h) and electron mobility (μ_e), as well as a decrease in the μ_h/μ_e ratio. Consequently, the PCE of devices without and with TCB is improved from 4.45% to 7.18%, which was a record for OPVs based on P3HT:O-IDTBR blends at that time.

Adjusting the temperature of the substrates can optimize the vertical phase separation of the active layer as well. Li et al. reported that optimized vertical phase separation can be obtained from hot spin processing [96]. The acceptor at the top surface of the blend films appears to be higher when the substrate temperature is raised from 20 to 80 °C. Be aware that the aggregation of polymer PM6 is temperature-dependent. Aggregates are formed by quickly quenching polymers in o-xy solution (80 °C) onto the cool substrate, and the solution's entangled polymers containing acceptors precipitate out of it. However, because of the decreased viscosity, the liquid residues on the film top evaporate quickly. Eventually, the top surface has few acceptors and comparatively thin coatings. The precipitation and aggregation processes of polymers are prolonged when utilizing a heated substrate (80 °C) because of the comparable temperature between the substrate and solution. This provides the delayed time needed for the formation of polymer gel networks to maintain their high viscosity in the liquid state, resulting in a thick active layer with a top surface rich

in acceptors. The active layer featuring an acceptor-rich top surface is perfect for exciton dissociation, charge transfer, and extraction, resulting in an excellent PCE of 18.25%.

3.2. Enhancing Crystallinity via Film-Forming Kinetics

High carrier mobility facilitates carrier transfer and collection in the photoelectric conversion processes of OPVs, which is conducive to device performance. The continuous band conduction model and the discontinuous hopping transport model are the two models used to describe charge transport in organic semiconductor materials [97]. Because conjugated molecules have weak interactions with one another, the charge transport model follows the hopping transport model. Marcus theorizes that high molecular crystallinity facilitates charge transmission [98]. Consequently, it is important to carefully regulate the active layer's crystallinity [84,99,100].

The kinetics of film formation, encompassing both the film-forming duration and crystallization consequence, significantly influence the crystallinity of films as well. Solvent engineering is an effective method to regulate the duration of film-forming process [93]. Take P3HT:O-IDTBR blends as an example, three groups are chosen based on their boiling points (bps) in relation to the primary solvent CB: chloroform (CF), with a lower bp; o-dichlorobenzene (DCB) and TCB, with higher bps; and chloronaphthalene (CN) with the highest pb. After adding cosolvents, the duration is shortened or lengthened, and grazing-incident wide-angle X-ray scattering (GIWAXS) indicates that the crystallinity of the P3HT:O-IDTBR film is regulated (Figure 3). The P3HT (100) signal remains for the CB-processed film; however, it becomes less intense than for the P3HT film. The addition of CF causes the P3HT diffraction signal to weaken, indicating a decrease in the crystallinity of P3HT. Furthermore, O-IDTBR's diffraction signal is too weak to be seen. The greater diffraction signals observed after adding DCB and TCB are ascribed to P3HT's increased crystallinity, and O-IDTBR's crystallinity is also improved. The diffraction of P3HT in the CN-fabricated film is very strong, and additional diffraction signals occur at $q = 0.596$ Å^{-1}, which could be the result of O-IDTBR's complex crystalline structure due to its improved crystallinity.

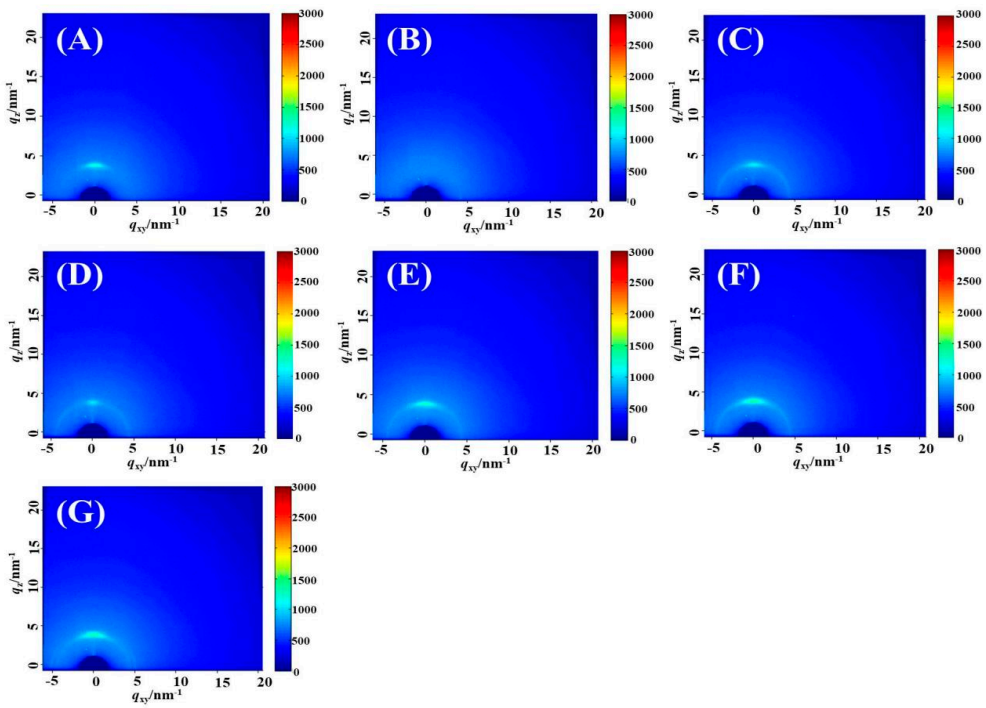

Figure 3. The GIWAXS patterns of P3HT (**A**), O-IDTBR films (**B**) and blend films fabricated by CB (**C**), CB with CF (**D**), CB with DCB (**E**), CB with TCB (**F**), CB with CN (**G**). Reproduced with per-mission from [93], ELSEVIER, 2020.

The duration of the film-forming can adjust the crystallinity. The entire film-forming time is reduced when the solvent with a low bp is added. The rapid solvent evaporation causes the diffusion of both the donor and acceptor molecules in the solution to be repressed, which in turn leads to a decrease in crystallinity. Because of the longer duration of the film-forming process when adding cosolvents with high bps, the donor and acceptor are able to adjust their molecular conformations and diffuse to the crystallographic frontier with sufficient time, resulting in the formation of relatively pure phases with a high crystallinity.

4. Optimizing Domain Size via Sequential Crystallization

The active layer's appropriate domain size is crucial in effective exciton dissociation and charge transport in OPVs [92]. Experiments and theoretical calculations show that the optimal domain size is approximately 10–20 nm, which is similar to the diffusion of excitons and advantageous for charge generation. However, achieving such a small domain size in all-polymer photovoltaics is very challenging, because in the last stages of the film-forming process both the donor and acceptor polymers can further crystallize due to their low glass transition temperature, which leads to the formation of a large domain size [101,102].

The driving force for phase separation is crystallization, so the sequential crystallization of polymer blends is proposed to reduce the domain size by inducing the donor and acceptor molecules to crystallize at different stages. To clarify the basic relationships between crystallization kinetics and domain size, the crystalline–crystalline blend system PBDB-T:N2200 is chosen. By combining the solution states and post-annealing, N2200 crystallizes during the film-forming process, while PBDB-T crystallizes in the post-annealing process, which lowers the driving force for phase separation, thus produces fine phase separation structures, as indicated in Scheme 1 [103].

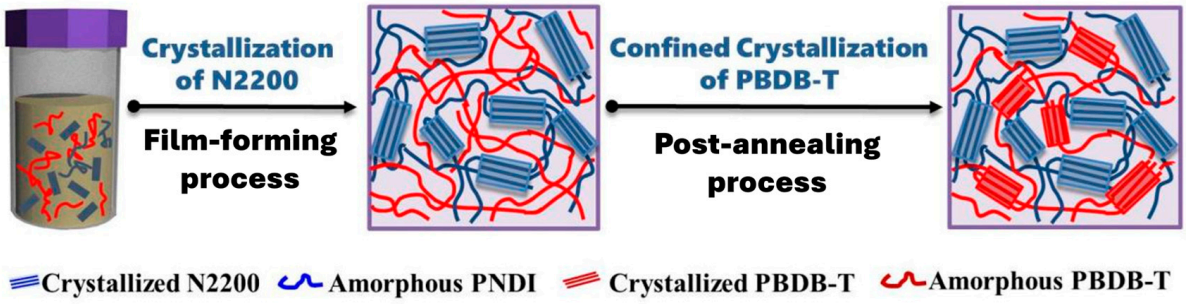

Scheme 1. Diagrammatic representation of sequential crystallization. Copyright 2022, the authors.

4.1. Combining Solution Temperature and Thermal Annealing

Both PBDB-T and N2200 have the tendency to produce pre-aggregates in solution due to their coplanarity. Because of the "memory effect", the pre-aggregates serve as the nucleus and drive both PBDB-T and N2200 to crystallize throughout the film-forming process, resulting in a significant phase separation [103,104]. according to solvent–polymer affinities (χ_{S-P}), as in Equation (1) [105]:

$$\chi_{s-p} = V\left(\Delta\delta_d^2 + 0.25\Delta\delta_p^2 + 0.25\Delta\delta_h^2\right)/RT \quad (1)$$

The solvent's molar volume is represented by V, while the polymer's and solvent's respective dispersion, polar, and hydrogen bonding solubility parameters are $\Delta\delta_d$, $\Delta\delta_p$, and $\Delta\delta_h$. T is the absolute temperature, while R is the gas constant.

It is well known that polymer chains prefer to interact with one another and form pre-aggregates when χ_{S-P} is large. While when χ_{S-P} is small, polymers are more likely to become molecularly distributed in the solvent. Therefore, by regulating the properties of the solvent or the solution's temperature, the pre-aggregation of polymer chains might be controlled.

Take regulating the solution temperature as an example, by adjusting the temperature, the PBDB-T:N2200 solution's pre-aggregation was controlled. The UV–vis spectra displayed in Figure 4A indicate that at room temperature PBDB-T substantially aggregates in CB solution. However, this aggregation may be successfully inhibited by raising the solution temperature above 80 °C. In a similar vein, Figure 4B shows the transition temperature (T_c) of N2200 in solution to be 95 °C. Hence, three distinct solution states can emerge in the PBDB-T:N2200 solution when the solution temperature is changed based on the different T_c's of N2200 and PBDB-T. Both PBDB-T and N2200 produce pre-aggregations in solution when the solution temperature of PBDB-T:N2200 blend is lower than the T_c of both PBDB-T and N2200. Only N2200 produces pre-aggregations if the solution temperature is between the T_c of PBDB-T and N2200. When the solution temperature is raised above the T_c of both PBDB-T and N2200, pre-aggregates cannot form for either PBDB-T or N2200.

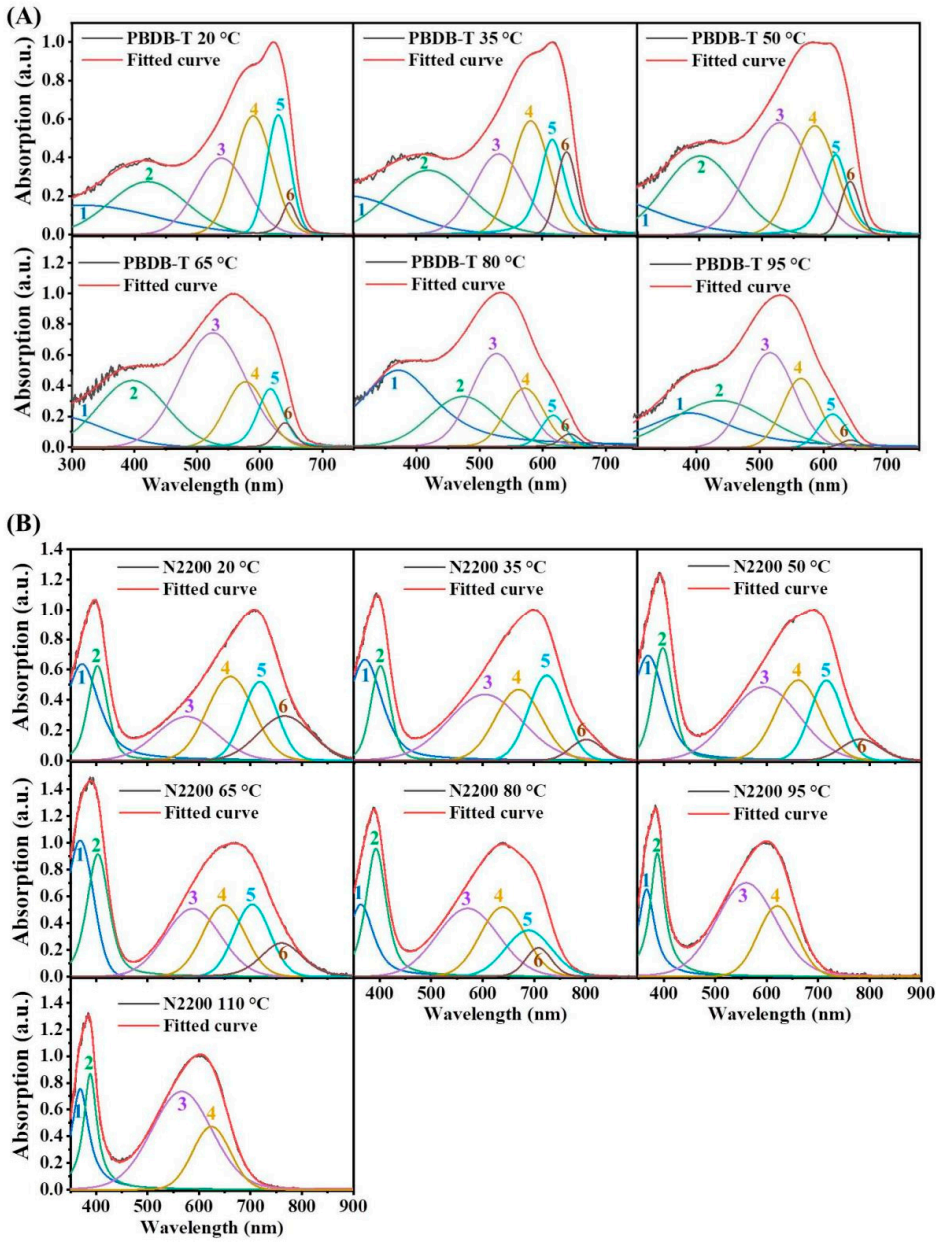

Figure 4. Absorption spectra of N2200 (**B**) and PBDB-T (**A**) in solution at various temperatures, both simulated and experimental (different colors represents different peak fit according to the absorption spectrum). Reproduced with permission from [103], ELSEVIER, 2022.

Phase separation is somewhat induced by crystallization [83,106]. Pre-aggregation occurs in solution for both PBDB-T and N2200 when the solution temperature is 20 °C. As seen in Figure 5A,B (route 1), both PBDB-T and N2200, therefore, have a tendency to crystallize during the film-forming process, which promotes large domains. On the other hand, neither PBDB-T nor N2200 will aggregate in solution when the temperature is higher than 95 °C. Because there is little driving force for phase separation, PBDB-T and N2200 have a tendency to develop an amorphous state during the film-forming process, which results in small domains (route 3). When the temperature of the solution falls between 80 °C and 95 °C, N2200 will aggregate and form pre-aggregates, PBDB-T chains tend to disperse in the amorphous state. Therefore, only N2200 can crystallize during the film-forming stage, creating a proper driving force for phase separation. As a result, route 2 is able to secure an appropriate domain size.

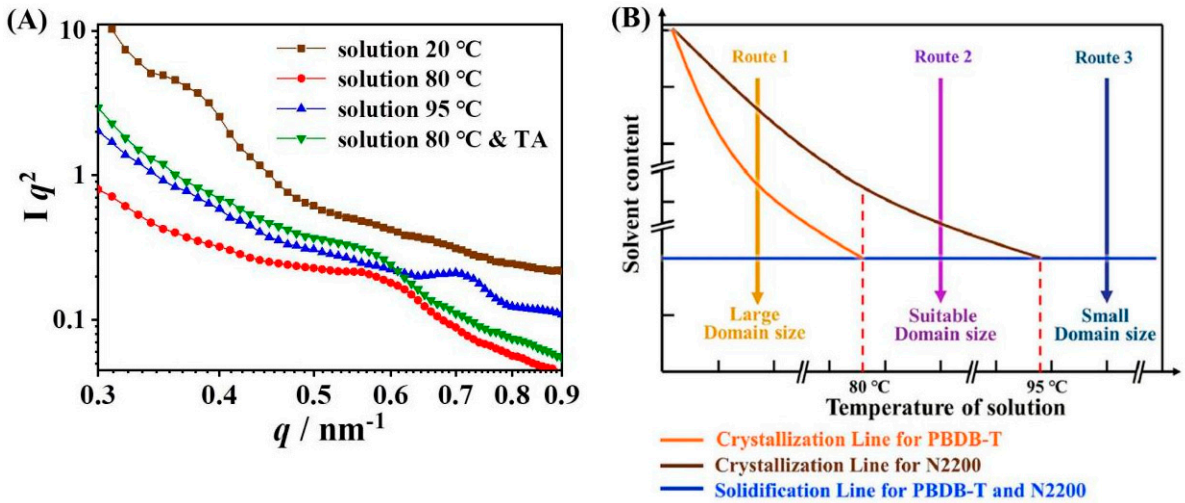

Figure 5. (**A**) The GISAXS spectra of film processed from solutions at 20 °C, 80 °C, and 95 °C, respectively; and the film exposed to TA treatment after being processed from solu-tion at 80 °C. (**B**) The phase diagram showing the various temperatures at which the PBDB-T:N2200 solution solidifies. Reproduced with permission from [103], ELSEVIER, 2022.

For route 2, PBDB-T chains in the active layer are nearly amorphous, despite the fact that the domain size is appropriate, which causes bimolecular recombination. To raise the crystallinity of PBDB-T on the premise of keeping the domain size unchanged, confined crystallization via thermal annealing (TA) is used. During the TA process, N2200 maintains its crystalline framework, and PBDB-T crystallizes under the confinement of N2200.

In order to carry out this procedure, an intricate selection of the annealing temperature is necessary. The findings demonstrate that the conformation of chain segments may adapt in N2200 crystallizing process when the temperature of TA ranges from 100 °C to 180 °C, leading to the confined crystallization of PBDB-T. In this instance, 140 °C is chosen as the temperature of TA. Following the TA process, PBDB-T's crystallinity considerably increases. As expect, grazing incidence small-angle X-ray scattering (GISAXS) (Figure 5) attests that the domain size remains virtually unaltered. Thus, by integrating the solution state with post-annealing, it is possible to modulate the kinetics of crystallization, and thus, fabricate crystalline active layers with an appropriate domain size.

This nano-structure of the active layer facilitates the exciton dissociation and promotes balanced charge transport, which results in a higher fill factor (FF) and short-circuit current density (J_{sc}) of 0.67 and 13.48 mA/cm^2, yielding a PCE of 7.59%. While the device based on the film processed from 20 °C only exhibits an FF and J_{sc} of 0.65 and 10.86 mA/cm^2, resulting in a lower PCE of 6.07%.

4.2. Combining Solution Temperature and Solvent Vapor Annealing

Combining solvent engineering and solvent vapor annealing (SVA) treatment can also regulate the crystallization consequences of the donor and acceptor in the blend. Take the PBDB-T:N2200 blend, for instance, the pre-aggregation extent of PBDB-T is suppressed via solvent engineering [104]. According to Flory–Huggins theory, χ_{S-P} can be adjusted by mixing solvents with different solubility parameters (δ). According to Equation (1), $\chi_{\text{CB-PBDB-T}}$ and $\chi_{\text{CB-N2200}}$ are 3.47×10^{-1} and 3.52×10^{-1}, respectively. As we mentioned in Section 3.1, reducing $\chi_{\text{polymer-solvent}}$ could suppress pre-aggregation of the polymer in solution.

To decrease $\chi_{\text{solvent-PBDB-T}}$ in this case, diphenyl ether (DPE), with a greater δ in comparison to PBDB-T, is added into the solution as an additive. Equation (2) is used to calculate the blended solvent's δ [107]:

$$\begin{aligned} \delta_{\text{Mixed}} &= \left(\delta^2_{\text{Mixed}-\text{d}} + \delta^2_{\text{Mixed}-\text{p}} + \delta^2_{\text{Mixed}-\text{h}}\right)^{1/2} \\ \delta_{\text{Mixed}-\text{d}} &= \varphi_1 \cdot \delta_{\text{d1}} + \varphi_2 \cdot \delta_{\text{d2}} \\ \delta_{\text{Mixed}-\text{p}} &= \varphi_1 \cdot \delta_{\text{p1}} + \varphi_2 \cdot \delta_{\text{p2}} \\ \delta_{\text{Mixed}-\text{h}} &= \varphi_1 \cdot \delta_{\text{h1}} + \varphi_2 \cdot \delta_{\text{h2}} \end{aligned} \tag{2}$$

where $\delta_{\text{Mixed}-\text{p}}$, $\delta_{\text{Mixed}-\text{h}}$, and $\delta_{\text{Mixed}-\text{d}}$ are the polar, hydrogen bonding, and dispersion solubility parameters for the mixed solvent, δ_{p}, δ_{h}, and δ_{d} are the polar, hydrogen bonding, and dispersion solubility parameters, respectively, and φ is the volume fraction. According to the outcome, DPE might be added to selectively inhibit PBDB-T pre-aggregation. After adding DPE, suppression of PBDB-T crystallization throughout the film-forming process results in a decrease in the driving force for phase separation and smaller domains.

SVA is a useful technique for increasing polymer films' crystallinity. Upon SVA, the polymer films are swollen, providing extra time for amorphous polymers to continue to self-organize. Here, CF is selected as solvent vapor, because PBDB-T films' can be enhanced in CF's SVA process, while N2200 is insensitive to CF's SVA process. Hence, after adding DPE and N2200 prior to crystallization in the film-forming process, the crystallization of PBDB-T occurs in the SVA process (Scheme 1).

As a result, as seen in Figure 6, a highly crystalline morphology with the appropriate domain size is produced by the SVA process with DPE. AFM and TEM are used to investigate the surface roughness and the phase separation structure. Figure 6A,a show that the film processed from a CB solution without DPE presents fibrous domains with a large scale and high crystallinity due to the interaction between donors and acceptors. For film processed from a CB solution with the high-boiling-point additive DPE, the PBDB-T's crystallization is inhibited by addition of the solvent, resulting in lots of N2200 fibers wrapped around by amorphous PBDB-T (Figure 6B,b), forming a crystalline framework with a small domain size. As seen in Figure 6C,c, after N2200 crystallizes, PBDB-T crystallizes during the followed SVA process while being confined by the N2200 framework, yielding a crystalline nano-structure with a modest domain size. Exciton diffusion, CT state dissociation, and charge transport all benefit from the improved morphology, which raises the PCE from 6.55% to 7.78%—the greatest PCE for OPVs that are based on the PBDB-T:N2200 blend at the moment. These two studies shed light on the connection between phase separation structures and crystallization kinetics, which could serve as a roadmap for precisely regulating the active layer's domain size in OPVs.

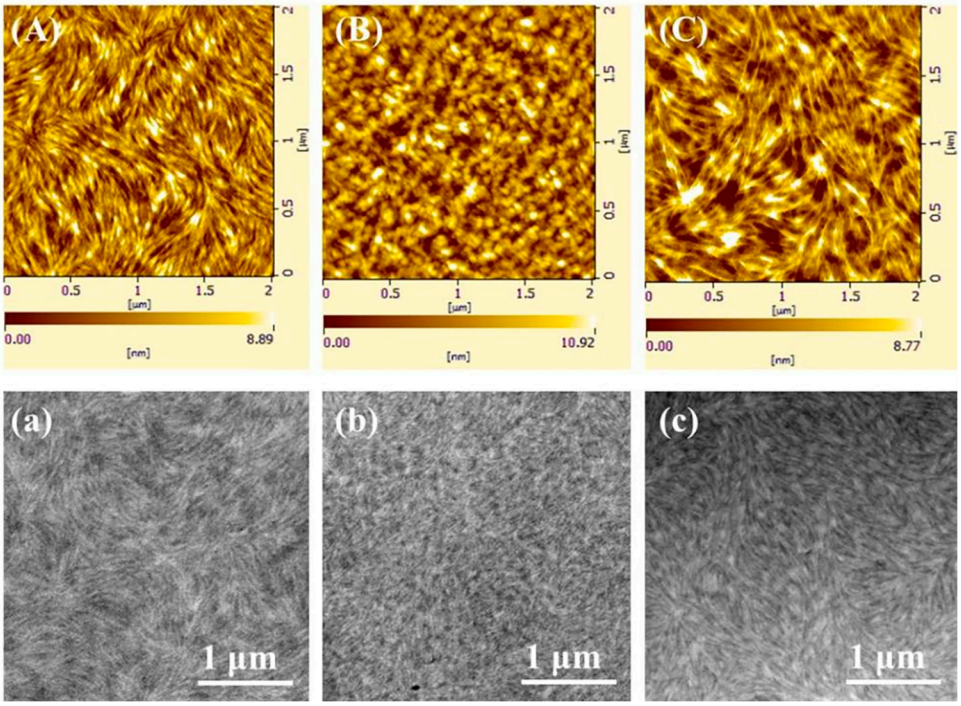

Figure 6. AFM and TEM images of PBDB-T:N2200 active layers: (**A**,**a**) processed from solutions without DPE, (**B**,**b**) processed from solutions with DPE, (**C**,**c**) cast from the solution with DPE and then treated by SVA [104]. Reproduced with permission from [104], American Chemical Society., 2020.

5. Regulating the Diffusivity to Adjust Molecular Orientation

Conjugated molecules are known to be anisotropic and to have edge-on, face-on, and flat-on molecular orientations. The charge transport and dissociation efficiency of the CT state are significantly influenced by the molecule orientation [108,109]. It is possible that conjugated molecules' electrical coupling can reduce the charge transport barrier [45]. Because of this, molecules oriented face-on may provide π-π electrical coupling along the direction perpendicular to the substrate, which is advantageous for charge transfer in OPVs. Furthermore, the intermolecular electric fields at the donor/acceptor interfaces will peak when the donor and acceptor adopt the same orientation, providing a powerful driving force to dissociate CT states [110–112]. Thus, in order to achieve good performance, it is highly desired for both donor and acceptor molecules to adopt face-on orientation in OPVs.

Epitaxial crystallization is a useful strategy for regulation the orientation through fine-tuning the interactions among different molecules. In the *p*-DTS(FBTTh$_2$)$_2$/PC$_{71}$BM blend, *p*-DTS(FBTTh$_2$)$_2$ molecules are more inclined to adopt an edge-on orientation. In order to induce the transition of the orientation from edge-on to face-on, Zhao et al. employed PTB7-Th, the polymer prefers the face-on orientation, to serve as a nucleus for the epitaxial crystallization of *p*-DTS(FBTTh$_2$)$_2$. PTB7-Th and *p*-DTS(FBTTh$_2$)$_2$ have a high degree of lattice matching, which caused *p*-DTS(FBTTh$_2$)$_2$ to tend to epitaxially grow on PTB7-Th's surface in the film-forming process. As a result, *p*-DTS(FBTTh$_2$)$_2$ exhibited a face-on orientation, which enhanced hole mobility and inhibited bimolecular recombination. This work only reveals the premise of thermodynamics for the transition of orientation, while the dynamic parameter is still unclear [113].

In order to figure out the kinetics parameters, the blended system DRCN5T:ITIC-Th was used as model system. DRCN5T favors the edge-on orientation in the DRCN5T:ITIC-Th blend, whereas ITIC-Th displays the face-on orientation [114,115]. To adjust DRCN5T's orientation, the authors chose N2200 as the third component for the following reasons from the thermodynamic aspect: firstly, the crystallinity of N2200 is high and its orientation is face-on; secondly, the lattice matching degree between N2200 and DRCN5T should be

greater than 90%; in addition, the miscibility between DRCN5T and N2200 is suitable. Thus, N2200 is a suitable candidate for inducing the orientation transition of DRCN5T.

Table 1. Table of regulation methods and corresponding results.

Regulation Methods and Corresponding Results						
Ref.	**Material System**		J_{SC} (mA cm^{-2})	V_{OC} (V)	**FF**	**PCE**
[91]	P3HT: O-IDTBR (CB)	Section 3.1 Regulation of bicontinuous structure				
		Without TCB → isolated spherical structures	8.81	0.77	0.64	4.45%
		With TCB → bicontinuous networks	13.49	0.76	0.70	7.18%
[93]	P3HT: O-IDTBR (CB)	Section 3.2 Regulation of crystallinity				
		Without additive → low crystallinity	9.34	0.77	0.64	4.60%
		With TCB → medium crystallinity	13.53	0.76	0.70	7.20%
		With CN → high crystallinity	10.01	0.76	0.70	5.32%
[104]	PBDB-T: N2200	Section 4 Regulation of domain size				
		Simultaneous crystallization → small domain size	11.46	0.84	0.65	6.55%
		Sequential crystallization → modest domain size	13.42	0.82	0.67	7.78%
[114]	DRCN5T: ITIC-Th	Section 5 Regulation of molecular orientation				
		Medium diffusion rate → face-on	7.94	0.94	0.41	3.06%
		Fast diffusion rate → edge-on	9.18	0.99	0.52	4.73%

In order to illuminate the key parameters in the kinetics, DRCN5T:ITIC-Th:N2200 films are subjected to TA. Only N2200 presents crystalline behavior and the majority of the DRCN5T is amorphous in the DRCN5T:ITIC-Th:N2200 film without and with TA under 70 °C, which is confirmed by the sole diffraction signals of N2200 in Figure 7. The strength of DRCN5T's (010) diffraction signals dramatically increases when the TA temperature is raised to 100 °C and 130 °C. This indicates that the TA treatment encourages DRCN5T to crystallize face-on, and its crystallinity increases when elevating the TA temperature. As the temperature of TA is raised further to 160 °C, lamellar stacking signals centered at 4.9° and 6.5° occur in addition to an increase in the intensity of the (010) diffraction peak. This indicates that some DRCN5T crystallized in an edge-on orientation at high temperatures rather than in a face-on orientation.

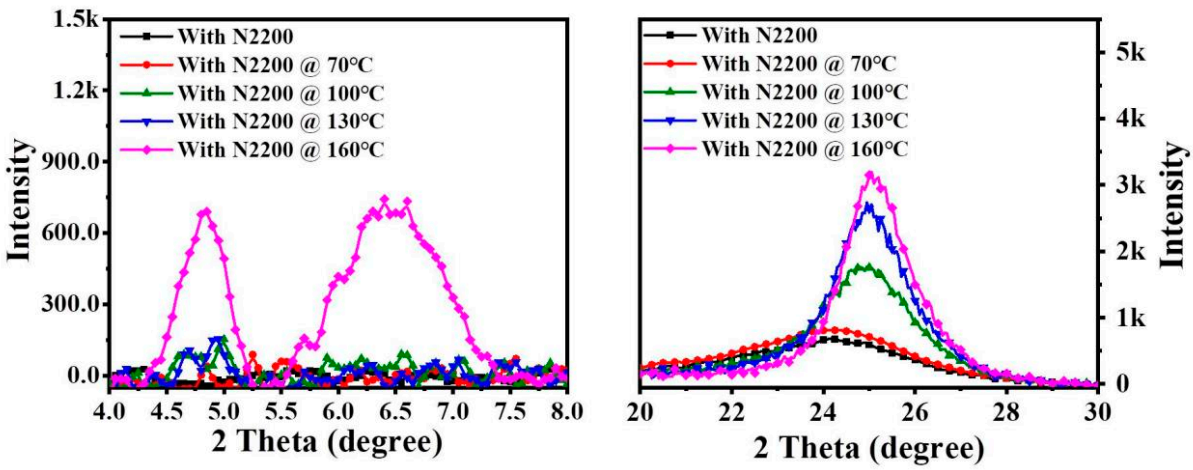

Figure 7. Out-of-plane grazing incidence X-ray diffraction (GIXD) patterns of DRCN5T:ITIC-Th:N2200 films under TA with different temperatures. Reproduced with permission from [113], WILEY-VCH, 2022.

The variable diffusivity of DRCN5T at different temperatures may account for the orientation variance. According to the Arrhenius equation (Equation (3)) [116], the diffusivity of molecules depends on temperature:

$$D = D_o \exp(-E_a/\mathrm{RT}) \quad (3)$$

where D is the diffusion coefficient, D_o is the temperature-independent frequency factor, R is the universal gas constant, T is the absolute temperature (in kelvin), and E_a is the activation energy. Since the diffusion coefficient is positively correlated with temperature, we can, thus, hypothesize that DRCN5T molecules diffuse easily at high temperatures. The diffusivity of DRCN5T is low at low TA temperatures (70 °C), which prevents it from passing the nucleation barrier. Consequently, DRCN5T would not crystallize, leaving its crystallinity and molecular orientation mostly unaltered. When the TA temperature rises to 100 °C or 130 °C, DRCN5T's diffusivity is increased, allowing DRCN5T to surpass the barrier for heterogeneous nucleation. Thus, DRCN5T shows epitaxial crystallization behavior on an N2200 surface, which promotes the orientation transition from edge-on to face-on. While DRCN5T exhibits edge-on orientation upon temperature rises to 160 °C, a phenomenon that can be attributed to homogeneous nucleation. It is well known that heterogeneous nucleation has a lower energy barrier than homogeneous nucleation. Because of this, at 160 °C the diffusivity of DRCN5T is so great that it can pass through both the heterogeneous and homogeneous nucleation energy barriers. As a result, by heterogeneous nucleation, DRCN5T near N2200 chains would attach to the surface of N2200 chains and undergo epitaxial crystallization, thus take on a face-on orientation. On the other hand, homogeneous nucleation would cause the DRCN5T far from N2200 to crystallize and take on an edge-on orientation, as shown in Scheme 2.

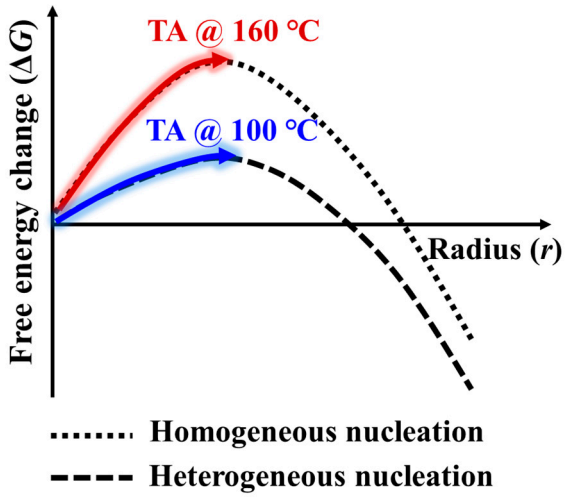

Scheme 2. Diagram illustrating the energetics of DRCN5T crystallization, where the y-axis represents the system's Gibbs free energy change (ΔG) and the x-axis represents the crystal radius (r) [113].

Consequently, DRCN5T's orientation changed from edge-on to face-on. A greater V_{oc} is the result of the optimized orientation suppressing the E_{loss} from 0.79 eV to 0.74 eV. Furthermore, the face-on orientation enhances carrier mobility and inhibits bimolecular recombination. As a result, the FF and J_{sc} are enhanced, and the PCE increases from 3.06% to 4.73%. These findings suggest that regulating the nucleation and diffusivity of molecules to maximize the content of face-on molecules could be a successful strategy for enhancing OPVs' performance.

6. Conclusions

In summary, this manuscript illustrates the influence of kinetics on the morphology of the active layer in OPVs. Moreover, strategies for optimizing the morphology of the active

layer via kinetic pathways are also introduced, including film-forming kinetics, sequential crystallization, and the molecular diffusion rate during the crystallization process. Integrating the above kinetics with thermodynamic factors, such as thermodynamic stability, L-L phase separation, the barriers of homogeneous and heterogeneous nucleation, the phase separation structure, crystallinity, domain size, and molecular orientation of the active layer are optimized in systems with different blends. On the base of fine morphology control, the relationship between the structure of the active layer and device performance is established, which lays the foundation for OPVs with high PCE.

Author Contributions: Conceptualization, J.L. and Z.H.; writing—original draft preparation, J.L. and L.W.; writing—review and editing, J.L. and L.W.; visualization, W.W. and M.J.; supervision, X.Y.; project administration, J.L.; funding acquisition, J.L. All authors have read and agreed to the published version of the manuscript.

Funding: This work was supported by the National Natural Science Foundation of China (52073231), the Shaanxi Provincial High level Talent Introduction Project (5113220044), the Shaanxi Outstanding Youth Project (2023-JC-JQ-33), the Youth Science and Technology Talent Promotion Project of Jiangsu Association for Science and Technology (TJ-2022-088), the National Aerospace Science Foundation of China (2020Z073053010), the Suzhou Science and Technology Development Plan Innovation Leading Talent Project (ZXL2023183), the Fundamental Research Funds for the Central Universities (G2023KY0605, G2023KY0601), the NWPU research fund for young scholars (G2022WD01014), the Natural Science Foundation of Chongqing, China (cstc2021jcyj-msxmX0990), the Basic Research Programs of Taicang (TC2021JC08), Guangdong Basic and Applied Basic Research Foundation (2024A1515012538), the Aeronautical Science Foundation of China (2018ZD53047, 2020Z073053010).

Conflicts of Interest: The authors declare no conflicts of interest.

References

1. Bi, P.; Zhang, S.; Ren, J.; Chen, Z.; Zheng, Z.; Cui, Y.; Wang, J.; Wang, S.; Zhang, T.; Li, J.; et al. A High-Performance Nonfused Wide-Bandgap Acceptor for Versatile Photovoltaic Applications. *Adv. Mater.* **2022**, *34*, e2108090. [CrossRef] [PubMed]
2. Cheng, P.; Li, G.; Zhan, X.; Yang, Y. Next-generation organic photovoltaics based on non-fullerene acceptors. *Nat. Photonics* **2018**, *12*, 131–142. [CrossRef]
3. Guo, J.; Min, J. A Cost Analysis of Fully Solution-Processed ITO-Free Organic Solar Modules. *Adv. Energy Mater.* **2018**, *9*, 1802521. [CrossRef]
4. Song, J.; Zhang, C.; Li, C.; Qiao, J.; Yu, J.; Gao, J.; Wang, X.; Hao, X.; Tang, Z.; Lu, G.; et al. Green-Solvent-Processed Organic Solar Cells with Approaching 20% Efficiency and Improved Photostability. *Angew. Chem. Int. Ed. Engl.* **2024**, e202404297. [CrossRef] [PubMed]
5. Yu, Y.; Sun, R.; Wang, T.; Yuan, X.; Wu, Y.; Wu, Q.; Shi, M.; Yang, W.; Jiao, X.; Min, J. Improving Photovoltaic Performance of Non-Fullerene Polymer Solar Cells Enables by Fine-Tuning Blend Microstructure via Binary Solvent Mixtures. *Adv. Funct. Mater.* **2020**, *31*, 2008767. [CrossRef]
6. Zhan, L.; Yin, S.; Li, Y.; Li, S.; Chen, T.; Sun, R.; Min, J.; Zhou, G.; Zhu, H.; Chen, Y.; et al. Multiphase Morphology with Enhanced Carrier Lifetime via Quaternary Strategy Enables High-Efficiency, Thick-Film, and Large-Area Organic Photovoltaics. *Adv. Mater.* **2022**, *34*, e2206269. [CrossRef]
7. Zhang, B.; Yang, F.; Li, Y. Recent Progress in Large-Area Organic Solar Cells. *Small Sci.* **2023**, *3*, 2300004. [CrossRef]
8. Li, C.; Zhou, J.; Song, J.; Xu, J.; Zhang, H.; Zhang, X.; Guo, J.; Zhu, L.; Wei, D.; Han, G.; et al. Non-fullerene acceptors with branched side chains and improved molecular packing to exceed 18% efficiency in organic solar cells. *Nat. Energy* **2021**, *6*, 605–613. [CrossRef]
9. Yi, J.; Zhang, G.; Yu, H.; Yan, H. Advantages, challenges and molecular design of different material types used in organic solar cells. *Nat. Rev. Mater.* **2023**, *9*, 46–62. [CrossRef]
10. Yuan, J.; Zhang, Y.; Zhou, L.; Zhang, G.; Yip, H.-L.; Lau, T.-K.; Lu, X.; Zhu, C.; Peng, H.; Johnson, P.A.; et al. Single-Junction Organic Solar Cell with over 15% Efficiency Using Fused-Ring Acceptor with Electron-Deficient Core. *Joule* **2019**, *3*, 1140–1151. [CrossRef]
11. Li, Y.; Liu, H.; Wu, J.; Tang, H.; Wang, H.; Yang, Q.; Fu, Y.; Xie, Z. Additive and High-Temperature Processing Boost the Photovoltaic Performance of Nonfullerene Organic Solar Cells Fabricated with Blade Coating and Nonhalogenated Solvents. *ACS Appl. Mater. Interfaces* **2021**, *13*, 10239–10248. [CrossRef] [PubMed]
12. Zhang, L.; Lin, B.; Hu, B.; Xu, X.; Ma, W. Blade-Cast Nonfullerene Organic Solar Cells in Air with Excellent Morphology, Efficiency, and Stability. *Adv. Mater.* **2018**, *30*, e1800343. [CrossRef]
13. Zhao, Y.; Wang, G.; Wang, Y.; Xiao, T.; Adil, M.A.; Lu, G.; Zhang, J.; Wei, Z. A Sequential Slot-Die Coated Ternary System Enables Efficient Flexible Organic Solar Cells. *Solar RRL* **2019**, *3*, 1800333. [CrossRef]

14. Liu, Y.; Liu, B.; Ma, C.-Q.; Huang, F.; Feng, G.; Chen, H.; Hou, J.; Yan, L.; Wei, Q.; Luo, Q.; et al. Recent progress in organic solar cells (Part II device engineering). *Sci. China Chem.* **2022**, *65*, 1457–1497. [CrossRef]
15. Zhou, Z.; Xu, S.; Song, J.; Jin, Y.; Yue, Q.; Qian, Y.; Liu, F.; Zhang, F.; Zhu, X. High-efficiency small-molecule ternary solar cells with a hierarchical morphology enabled by synergizing fullerene and non-fullerene acceptors. *Nature Energy* **2018**, *3*, 952–959. [CrossRef]
16. Liu, B.; Xu, Y.; Xia, D.; Xiao, C.; Yang, Z.; Li, W. Semitransparent Organic Solar Cells based on Non-Fullerene Electron Acceptors. *Acta Phys. Chim. Sin.* **2020**, *37*, 2009056. [CrossRef]
17. Liang, Q.; Lu, H.; Chang, Y.; He, Z.; Zhao, Y.; Liu, J. Morphology Control in Organic Solar Cells. *Energies* **2022**, *15*, 5344. [CrossRef]
18. Liu, J.; Wang, E.; Zhao, K. Editorial: Polymer Solar Cells: Molecular Design and Microstructure Control. *Front. Chem.* **2020**, *8*, 697. [CrossRef]
19. Li, Y. All-Small-Molecule Organic Solar Cells: Hierarchical Morphology Control Achieves Efficiency Breakthrough. *Acta Phys. Chim. Sin.* **2020**, *36*, 2001011. [CrossRef]
20. Gao, W.; Qi, F.; Peng, Z.; Lin, F.R.; Jiang, K.; Zhong, C.; Kaminsky, W.; Guan, Z.; Lee, C.S.; Marks, T.J.; et al. Achieving 19% Power Conversion Efficiency in Planar-Mixed Heterojunction Organic Solar Cells Using a Pseudosymmetric Electron Acceptor. *Adv. Mater.* **2022**, *34*, e2202089. [CrossRef]
21. Sun, R.; Wu, Y.; Yang, X.; Gao, Y.; Chen, Z.; Li, K.; Qiao, J.; Wang, T.; Guo, J.; Liu, C.; et al. Single-Junction Organic Solar Cells with 19.17% Efficiency Enabled by Introducing One Asymmetric Guest Acceptor. *Adv. Mater.* **2022**, *34*, e2110147. [CrossRef] [PubMed]
22. Wei, Y.; Chen, Z.; Lu, G.; Yu, N.; Li, C.; Gao, J.; Gu, X.; Hao, X.; Lu, G.; Tang, Z.; et al. Binary Organic Solar Cells Breaking 19% via Manipulating the Vertical Component Distribution. *Adv. Mater.* **2022**, *34*, e2204718. [CrossRef]
23. He, C.; Pan, Y.; Ouyang, Y.; Shen, Q.; Gao, Y.; Yan, K.; Fang, J.; Chen, Y.; Ma, C.-Q.; Min, J.; et al. Manipulating the D:A interfacial energetics and intermolecular packing for 19.2% efficiency organic photovoltaics. *Energy Environ. Sci.* **2022**, *15*, 2537–2544. [CrossRef]
24. Bhattacharya, S.; John, S. Beyond 30% Conversion Efficiency in Silicon Solar Cells: A Numerical Demonstration. *Sci. Rep.* **2019**, *9*, 12482. [CrossRef]
25. Shen, Z.; Han, Q.; Luo, X.; Shen, Y.; Wang, Y.; Yuan, Y.; Zhang, Y.; Yang, Y.; Han, L. Efficient and stable perovskite solar cells with regulated depletion region. *Nat. Photonics* **2024**. [CrossRef]
26. Sun, K.; Xiao, P.; Dumur, F.; Lalevée, J. Organic dye-based photoinitiating systems for visible-light-induced photopolymerization. *J. Polym. Sci.* **2021**, *59*, 1338–1389. [CrossRef]
27. Liu, J.; Liu, X.; Xin, J.; Zhang, Y.; Wen, L.; Liang, Q.; Miao, Z. Dual Function of the Third Component in Ternary Organic Solar Cells: Broaden the Spectrum and Optimize the Morphology. *Small* **2024**, e2308863. [CrossRef] [PubMed]
28. Tang, H.; Bai, Y.; Zhao, H.; Qin, X.; Hu, Z.; Zhou, C.; Huang, F.; Cao, Y. Interface Engineering for Highly Efficient Organic Solar Cells. *Adv. Mater.* **2024**, *36*, e2212236. [CrossRef]
29. Kim, H.K.; Yu, H.; Pan, M.; Shi, X.; Zhao, H.; Qi, Z.; Liu, W.; Ma, W.; Yan, H.; Chen, S. Linker Unit Modulation of Polymer Acceptors Enables Highly Efficient Air-Processed All-Polymer Solar Cells. *Adv. Sci.* **2022**, *9*, e2202223. [CrossRef]
30. Gurney, R.S.; Lidzey, D.G.; Wang, T. A review of non-fullerene polymer solar cells: From device physics to morphology control. *Rep. Prog. Phys.* **2019**, *82*, 036601. [CrossRef]
31. Xie, B.; Chen, Z.; Ying, L.; Huang, F.; Cao, Y. Near-infrared organic photoelectric materials for light-harvesting systems: Organic photovoltaics and organic photodiodes. *InfoMat* **2019**, *2*, 57–91. [CrossRef]
32. Wang, Y.; Xue, J.; Zhong, H.; Everett, C.R.; Jiang, X.; Reus, M.A.; Chumakov, A.; Roth, S.V.; Adedeji, M.A.; Jili, N.; et al. Control of the Crystallization and Phase Separation Kinetics in Sequential Blade-Coated Organic Solar Cells by Optimizing the Upper Layer Processing Solvent. *Adv. Energy Mater.* **2023**, *13*, 2203496. [CrossRef]
33. Weng, K.; Ye, L.; Zhu, L.; Xu, J.; Zhou, J.; Feng, X.; Lu, G.; Tan, S.; Liu, F.; Sun, Y. Optimized active layer morphology toward efficient and polymer batch insensitive organic solar cells. *Nat. Commun.* **2020**, *11*, 2855. [CrossRef] [PubMed]
34. Zhu, L.; Zhong, W.; Qiu, C.; Lyu, B.; Zhou, Z.; Zhang, M.; Song, J.; Xu, J.; Wang, J.; Ali, J.; et al. Aggregation-Induced Multilength Scaled Morphology Enabling 11.76% Efficiency in All-Polymer Solar Cells Using Printing Fabrication. *Adv. Mater.* **2019**, *31*, e1902899. [CrossRef] [PubMed]
35. Ye, L.; Collins, B.A.; Jiao, X.; Zhao, J.; Yan, H.; Ade, H. Miscibility–Function Relations in Organic Solar Cells: Significance of Optimal Miscibility in Relation to Percolation. *Adv. Energy Mater.* **2018**, *8*, 1703058. [CrossRef]
36. Ye, L.; Hu, H.; Ghasemi, M.; Wang, T.; Collins, B.A.; Kim, J.H.; Jiang, K.; Carpenter, J.H.; Li, H.; Li, Z.; et al. Quantitative relations between interaction parameter, miscibility and function in organic solar cells. *Nat. Mater.* **2018**, *17*, 253–260. [CrossRef] [PubMed]
37. Yang, H.; Bao, S.; Cui, N.; Fan, H.; Hu, K.; Cui, C.; Li, Y. Morphology Optimization of the Photoactive Layer through Crystallinity and Miscibility Regulation for High-performance Polymer Solar Cells. *Angew. Chem. Int. Ed. Engl.* **2023**, *62*, e202216338. [CrossRef] [PubMed]
38. Jiao, X.; Ye, L.; Ade, H. Quantitative Morphology–Performance Correlations in Organic Solar Cells: Insights from Soft X-ray Scattering. *Adv. Energy Mater.* **2017**, *7*, 1700084. [CrossRef]
39. Neupane, U.; Bahrami, B.; Biesecker, M.; Baroughi, M.F.; Qiao, Q. Kinetic Monte Carlo modeling on organic solar cells: Domain size, donor-acceptor ratio and thickness. *Nano Energy* **2017**, *35*, 128–137. [CrossRef]
40. Sajjad, M.T.; Ruseckas, A.; Samuel, I.D.W. Enhancing Exciton Diffusion Length Provides New Opportunities for Organic Photovoltaics. *Matter* **2020**, *3*, 341–354. [CrossRef]

41. Lee, H.; Lee, D.; Sin, D.H.; Kim, S.W.; Jeong, M.S.; Cho, K. Effect of donor–acceptor molecular orientation on charge photogeneration in organic solar cells. *NPG Asia Mater.* **2018**, *10*, 469–481. [CrossRef]
42. Li, W.; Chen, M.; Cai, J.; Spooner, E.L.K.; Zhang, H.; Gurney, R.S.; Liu, D.; Xiao, Z.; Lidzey, D.G.; Ding, L.; et al. Molecular Order Control of Non-fullerene Acceptors for High-Efficiency Polymer Solar Cells. *Joule* **2019**, *3*, 819–833. [CrossRef]
43. Ma, Y.; Zhang, M.; Wan, S.; Yin, P.; Wang, P.; Cai, D.; Liu, F.; Zheng, Q. Efficient Organic Solar Cells from Molecular Orientation Control of M-Series Acceptors. *Joule* **2021**, *5*, 197–209. [CrossRef]
44. Ye, L.; Weng, K.; Xu, J.; Du, X.; Chandrabose, S.; Chen, K.; Zhou, J.; Han, G.; Tan, S.; Xie, Z.; et al. Unraveling the influence of non-fullerene acceptor molecular packing on photovoltaic performance of organic solar cells. *Nat. Commun.* **2020**, *11*, 6005. [CrossRef]
45. Liang, Q.; Duan, M.; Geng, Z.; Zhang, M.; Xu, W.; Geng, H.; He, Z.; Liu, J. Regulation of molecular orientation in organic solar cells. *Chem. Eng. J.* **2024**, *488*, 150783. [CrossRef]
46. Dong, Y.; Nikolis, V.C.; Talnack, F.; Chin, Y.C.; Benduhn, J.; Londi, G.; Kublitski, J.; Zheng, X.; Mannsfeld, S.C.B.; Spoltore, D.; et al. Orientation dependent molecular electrostatics drives efficient charge generation in homojunction organic solar cells. *Nat. Commun.* **2020**, *11*, 4617. [CrossRef] [PubMed]
47. Heumueller, T.; Mateker, W.R.; Sachs-Quintana, I.T.; Vandewal, K.; Bartelt, J.A.; Burke, T.M.; Ameri, T.; Brabec, C.J.; McGehee, M.D. Reducing burn-in voltage loss in polymer solar cells by increasing the polymer crystallinity. *Energy Environ. Sci.* **2014**, *7*, 2974–2980. [CrossRef]
48. Hu, H.; Li, Y.; Zhang, J.; Peng, Z.; Ma, L.k.; Xin, J.; Huang, J.; Ma, T.; Jiang, K.; Zhang, G.; et al. Effect of Ring-Fusion on Miscibility and Domain Purity: Key Factors Determining the Performance of PDI-Based Nonfullerene Organic Solar Cells. *Adv. Energy Mater.* **2018**, *8*, 18000234. [CrossRef]
49. Liang, Q.; Hu, Z.; Yao, J.; Wu, Z.; Ding, Z.; Zhao, K.; Jiao, X.; Liu, J.; Huang, W. Blending Donors with Different Molecular Weights: An Efficient Strategy to Resolve the Conflict between Coherence Length and Intermixed Phase in Polymer/Nonfullerene Solar Cells. *Small* **2022**, *18*, e2103804. [CrossRef]
50. Zhong, W.; Zhang, M.; Zhu, L.; Zhang, Y.; Liu, F. Complex multilength-scale morphology in organic photovoltaics. *Trends Chem.* **2022**, *4*, 699–713. [CrossRef]
51. Huang, Y.; Kramer, E.J.; Heeger, A.J.; Bazan, G.C. Bulk heterojunction solar cells: Morphology and performance relationships. *Chem. Rev.* **2014**, *114*, 7006–7043. [CrossRef] [PubMed]
52. He, X.; Chan, C.C.S.; Kim, J.; Liu, H.; Su, C.J.; Jeng, U.S.; Su, H.; Lu, X.; Wong, K.S.; Choy, W.C.H. 1-Chloronaphthalene-Induced Donor/Acceptor Vertical Distribution and Carrier Dynamics Changes in Nonfullerene Organic Solar Cells and the Governed Mechanism. *Small Methods* **2022**, *6*, e2101475. [CrossRef] [PubMed]
53. Jee, M.H.; Ryu, H.S.; Lee, D.; Lee, W.; Woo, H.Y. Recent Advances in Nonfullerene Acceptor-Based Layer-by-Layer Organic Solar Cells Using a Solution Process. *Adv. Sci.* **2022**, *9*, e2201876. [CrossRef]
54. Liang, Q.; Hu, Z.; Yao, J.; Yin, Y.; Wei, P.; Chen, Z.; Li, W.; Liu, J. Recent advances in intermixed phase of organic solar cells: Characterization, regulating strategies and device applications. *J. Polym. Sci.* **2021**, *60*, 917–944. [CrossRef]
55. Liang, Q.; Yao, J.; Hu, Z.; Wei, P.; Lu, H.; Yin, Y.; Wang, K.; Liu, J. Recent Advances of Film–Forming Kinetics in Organic Solar Cells. *Energies* **2021**, *14*, 7604. [CrossRef]
56. Liu, J.; Zhang, Y.; Liu, X.; Wen, L.; Wan, L.; Song, C.; Xin, J.; Liang, Q. Solution Sequential Deposition Pseudo-Planar Heterojunction: An Efficient Strategy for State-of-Art Organic Solar Cells. *Small Methods* **2024**, e2301803. [CrossRef]
57. Qin, Y.; Xu, Y.; Peng, Z.; Hou, J.; Ade, H. Low Temperature Aggregation Transitions in N3 and Y6 Acceptors Enable Double-Annealing Method That Yields Hierarchical Morphology and Superior Efficiency in Nonfullerene Organic Solar Cells. *Adv. Funct. Mater.* **2020**, *30*, 2005011. [CrossRef]
58. Bin, H.; Zhang, Z.G.; Gao, L.; Chen, S.; Zhong, L.; Xue, L.; Yang, C.; Li, Y. Non-Fullerene Polymer Solar Cells Based on Alkylthio and Fluorine Substituted 2D-Conjugated Polymers Reach 9.5% Efficiency. *J. Am. Chem. Soc.* **2016**, *138*, 4657–4664. [CrossRef] [PubMed]
59. Min, J.; Güldal, N.S.; Guo, J.; Fang, C.; Jiao, X.; Hu, H.; Heumüller, T.; Ade, H.; Brabec, C.J. Gaining further insight into the effects of thermal annealing and solvent vapor annealing on time morphological development and degradation in small molecule solar cells. *J. Mater. Chem. A* **2017**, *5*, 18101–18110. [CrossRef]
60. Liu, B.; Sun, H.; Lee, J.W.; Jiang, Z.; Qiao, J.; Wang, J.; Yang, J.; Feng, K.; Liao, Q.; An, M.; et al. Efficient and stable organic solar cells enabled by multicomponent photoactive layer based on one-pot polymerization. *Nat. Commun.* **2023**, *14*, 967. [CrossRef]
61. Qiao, X.-L.; Yang, J.; Han, L.-H.; Zhang, J.-D.; Zhu, M.-F. Synergistic Effects of Solvent Vapor Assisted Spin-coating and Thermal Annealing on Enhancing the Carrier Mobility of Poly(3-hexylthiophene) Field-effect Transistors. *Chin. J. Polym. Sci.* **2021**, *39*, 849–855. [CrossRef]
62. Ge, J.; Hong, L.; Song, W.; Xie, L.; Zhang, J.; Chen, Z.; Yu, K.; Peng, R.; Zhang, X.; Ge, Z. Solvent Annealing Enables 15.39% Efficiency All-Small-Molecule Solar Cells through Improved Molecule Interconnection and Reduced Non-Radiative Loss. *Adv. Energy Mater.* **2021**, *11*, 2100800. [CrossRef]
63. Harreiß, C.; Langner, S.; Wu, M.; Berlinghof, M.; Rechberger, S.; Will, J.; Conroy, M.; Bangert, U.; Unruh, T.; Brabec, C.J.; et al. Understanding and Controlling the Evolution of Nanomorphology and Crystallinity of Organic Bulk-Heterojunction Blends with Solvent Vapor Annealing. *Solar RRL* **2022**, *6*, 2200127. [CrossRef]

64. Zhao, H.; Naveed, H.B.; Lin, B.; Zhou, X.; Yuan, J.; Zhou, K.; Wu, H.; Guo, R.; Scheel, M.A.; Chumakov, A.; et al. Hot Hydrocarbon-Solvent Slot-Die Coating Enables High-Efficiency Organic Solar Cells with Temperature-Dependent Aggregation Behavior. *Adv. Mater.* **2020**, *32*, e2002302. [CrossRef]
65. Chen, H.; Zhang, R.; Chen, X.; Zeng, G.; Kobera, L.; Abbrent, S.; Zhang, B.; Chen, W.; Xu, G.; Oh, J.; et al. A guest-assisted molecular-organization approach for >17% efficiency organic solar cells using environmentally friendly solvents. *Nat. Energy* **2021**, *6*, 1045–1053. [CrossRef]
66. Chen, L.; Ma, R.; Yi, J.; Dela Peña, T.A.; Li, H.; Wei, Q.; Yan, C.; Wu, J.; Li, M.; Cheng, P.; et al. Exploiting the donor-acceptor-additive interaction's morphological effect on the performance of organic solar cells. *Aggregate* **2023**, *5*, e455. [CrossRef]
67. Doumon, N.Y.; Wang, G.; Qiu, X.; Minnaard, A.J.; Chiechi, R.C.; Koster, L.J.A. 1,8-diiodooctane acts as a photo-acid in organic solar cells. *Sci. Rep.* **2019**, *9*, 4350. [CrossRef]
68. Liu, X.; Ma, R.; Wang, Y.; Du, S.; Tong, J.; Shi, X.; Li, J.; Bao, X.; Xia, Y.; Liu, T.; et al. Significantly Boosting Efficiency of Polymer Solar Cells by Employing a Nontoxic Halogen-Free Additive. *ACS Appl. Mater. Interfaces* **2021**, *13*, 11117–11124. [CrossRef]
69. Wang, Z.; Gao, K.; Kan, Y.; Zhang, M.; Qiu, C.; Zhu, L.; Zhao, Z.; Peng, X.; Feng, W.; Qian, Z.; et al. The coupling and competition of crystallization and phase separation, correlating thermodynamics and kinetics in OPV morphology and performances. *Nat. Commun.* **2021**, *12*, 332. [CrossRef]
70. Shen, Z.; Yu, J.; Lu, G.; Wu, K.; Wang, Q.; Bu, L.; Liu, X.; Zhu, Y.; Lu, G. Surface crystallinity enhancement in organic solar cells induced by spinodal demixing of acceptors and additives. *Energy Environ. Sci.* **2023**, *16*, 2945–2956. [CrossRef]
71. Xu, X.; Li, Y.; Peng, Q. Ternary Blend Organic Solar Cells: Understanding the Morphology from Recent Progress. *Adv. Mater.* **2022**, *34*, e2107476. [CrossRef]
72. Zhu, L.; Zhang, M.; Zhong, W.; Leng, S.; Zhou, G.; Zou, Y.; Su, X.; Ding, H.; Gu, P.; Liu, F.; et al. Progress and prospects of the morphology of non-fullerene acceptor based high-efficiency organic solar cells. *Energy Environ. Sci.* **2021**, *14*, 4341–4357. [CrossRef]
73. Sun, X.; Lv, J.; Zhang, C.; Wang, K.; Yang, C.; Hu, H.; Ouyang, X. Morphology Controlling of All-Small-Molecule Organic Solar Cells: From Donor Material Design to Device Engineering. *Solar RRL* **2023**, *7*, 2300332. [CrossRef]
74. Gao, H.; Sun, Y.; Meng, L.; Han, C.; Wan, X.; Chen, Y. Recent Progress in All-Small-Molecule Organic Solar Cells. *Small* **2023**, *19*, e2205594. [CrossRef] [PubMed]
75. Han, C.; Wang, J.; Chen, L.; Chen, J.; Zhou, L.; Wang, P.; Shen, W.; Zheng, N.; Wen, S.; Li, Y.; et al. Balancing Intermolecular Interactions between Acceptors and Donor/Acceptor for Efficient Organic Photovoltaics. *Adv. Funct. Mater.* **2021**, *31*, 2107026. [CrossRef]
76. Fu, J.; Fong, P.W.K.; Liu, H.; Huang, C.S.; Lu, X.; Lu, S.; Abdelsamie, M.; Kodalle, T.; Sutter-Fella, C.M.; Yang, Y.; et al. 19.31% binary organic solar cell and low non-radiative recombination enabled by non-monotonic intermediate state transition. *Nat. Commun.* **2023**, *14*, 1760. [CrossRef] [PubMed]
77. Dibb, G.F.; Jamieson, F.C.; Maurano, A.; Nelson, J.; Durrant, J.R. Limits on the Fill Factor in Organic Photovoltaics: Distinguishing Nongeminate and Geminate Recombination Mechanisms. *J. Chem. Phys. Lett.* **2013**, *4*, 803–808. [CrossRef] [PubMed]
78. Xiang, W.; Liu, S.F.; Tress, W. Interfaces and Interfacial Layers in Inorganic Perovskite Solar Cells. *Angew. Chem. Int. Ed. Engl.* **2021**, *60*, 26440–26453. [CrossRef]
79. Meng, B.; Fu, Y.; Xie, Z.; Liu, J.; Wang, L. Phosphonate-Functionalized Donor Polymer as an Underlying Interlayer To Improve Active Layer Morphology in Polymer Solar Cells. *Macromolecules* **2014**, *47*, 6246–6251. [CrossRef]
80. Wang, J.; Zheng, Z.; Zhang, D.; Zhang, J.; Zhou, J.; Liu, J.; Xie, S.; Zhao, Y.; Zhang, Y.; Wei, Z.; et al. Regulating Bulk-Heterojunction Molecular Orientations through Surface Free Energy Control of Hole-Transporting Layers for High-Performance Organic Solar Cells. *Adv. Mater.* **2019**, *31*, e1806921. [CrossRef]
81. Zheng, Z.; Zhang, S.; Wang, J.; Zhang, J.; Zhang, D.; Zhang, Y.; Wei, Z.; Tang, Z.; Hou, J.; Zhou, H. Exquisite modulation of ZnO nanoparticle electron transporting layer for high-performance fullerene-free organic solar cell with inverted structure. *J. Mater. Chem. A* **2019**, *7*, 3570–3576. [CrossRef]
82. Liang, Q.; Han, J.; Song, C.; Wang, Z.; Xin, J.; Yu, X.; Xie, Z.; Ma, W.; Liu, J.; Han, Y. Tuning molecule diffusion to control the phase separation of the p-DTS(FBTTh2)2/EP-PDI blend system via thermal annealing. *J. Mater. Chem. C* **2017**, *5*, 6842–6851. [CrossRef]
83. Liang, Q.; Han, J.; Song, C.; Yu, X.; Smilgies, D.-M.; Zhao, K.; Liu, J.; Han, Y. Reducing the confinement of PBDB-T to ITIC to improve the crystallinity of PBDB-T/ITIC blends. *J. Mater. Chem. A* **2018**, *6*, 15610–15620. [CrossRef]
84. Liu, J.; Han, J.; Liang, Q.; Xin, J.; Tang, Y.; Ma, W.; Yu, X.; Han, Y. Balancing Crystal Size in Small-Molecule Nonfullerene Solar Cells through Fine-Tuning the Film-Forming Kinetics to Fabricate Interpenetrating Network. *ACS Omega* **2018**, *3*, 7603–7612. [CrossRef] [PubMed]
85. Liang, Q.; Chang, Y.; Liang, C.; Zhu, H.; Guo, Z.; Liu, J. Application of Crystallization Kinetics Strategy in Morphology Control of Solar Cells Based on Nonfullerene Blends. *Acta Phys. Chim. Sin.* **2023**, *39*, 2212006. [CrossRef]
86. Zhao, L.; Wang, H.; Ji, H.; Li, S.; Miao, X.; Zhu, C.; Wang, W.; Huang, D.; Dong, X. A review on smart strategies for active layer phase separation regulation of organic solar cells. *APL Mater.* **2023**, *11*, 120601. [CrossRef]
87. Chen, L.; Yi, J.; Ma, R.; Ding, L.; Dela Pena, T.A.; Liu, H.; Chen, J.; Zhang, C.; Zhao, C.; Lu, W.; et al. An Isomeric Solid Additive Enables High-Efficiency Polymer Solar Cells Developed Using a Benzo-Difuran-Based Donor Polymer. *Adv. Mater.* **2023**, *35*, e2301231. [CrossRef]

88. Zhu, L.; Zhang, M.; Xu, J.; Li, C.; Yan, J.; Zhou, G.; Zhong, W.; Hao, T.; Song, J.; Xue, X.; et al. Single-junction organic solar cells with over 19% efficiency enabled by a refined double-fibril network morphology. *Nat. Mater.* **2022**, *21*, 656–663. [CrossRef]
89. Lin, B.; Zhou, X.; Zhao, H.; Yuan, J.; Zhou, K.; Chen, K.; Wu, H.; Guo, R.; Scheel, M.A.; Chumakov, A.; et al. Balancing the pre-aggregation and crystallization kinetics enables high efficiency slot-die coated organic solar cells with reduced non-radiative recombination losses. *Energy Environ. Sci.* **2020**, *13*, 2467–2479. [CrossRef]
90. Zhan, J.; Wang, L.; Zhang, M.; Zhu, L.; Hao, T.; Zhou, G.; Zhou, Z.; Chen, J.; Zhong, W.; Qiu, C.; et al. Manipulating Crystallization Kinetics of Conjugated Polymers in Nonfullerene Photovoltaic Blends toward Refined Morphologies and Higher Performances. *Macromolecules* **2021**, *54*, 4030–4041. [CrossRef]
91. Liang, Q.; Jiao, X.; Yan, Y.; Xie, Z.; Lu, G.; Liu, J.; Han, Y. Separating Crystallization Process of P3HT and O-IDTBR to Construct Highly Crystalline Interpenetrating Network with Optimized Vertical Phase Separation. *Adv. Funct. Mater.* **2019**, *29*, 1807591. [CrossRef]
92. Ye, L.; Li, S.; Liu, X.; Zhang, S.; Ghasemi, M.; Xiong, Y.; Hou, J.; Ade, H. Quenching to the Percolation Threshold in Organic Solar Cells. *Joule* **2019**, *3*, 443–458. [CrossRef]
93. Liu, J.; Zeng, S.; Jing, P.; Zhao, K.; Liang, Q. Investigating the effect of cosolvents on P3HT/O-IDTBR film-forming kinetics and film morphology. *J. Energy Chem.* **2020**, *51*, 333–341. [CrossRef]
94. Liang, Z.; Li, M.; Wang, Q.; Qin, Y.; Stuard, S.J.; Peng, Z.; Deng, Y.; Ade, H.; Ye, L.; Geng, Y. Optimization Requirements of Efficient Polythiophene:Nonfullerene Organic Solar Cells. *Joule* **2020**, *4*, 1278–1295. [CrossRef]
95. Fanta, G.M.; Jarka, P.; Szeluga, U.; Tanski, T.; Kim, J.Y. Phase Behavior of Amorphous/Semicrystalline Conjugated Polymer Blends. *Polymers* **2020**, *12*, 1726. [CrossRef]
96. Wang, D.; Zhou, G.; Li, Y.; Yan, K.; Zhan, L.; Zhu, H.; Lu, X.; Chen, H.; Li, C.Z. High-Performance Organic Solar Cells from Non-Halogenated Solvents. *Adv. Funct. Mater.* **2021**, *32*, 2107827. [CrossRef]
97. Torsi, L.; Dodabalapur, A.; Rothberg, L.J.; Fung, A.W.P.; Katz, H.E. Intrinsic Transport Properties and Performance Limits of Organic Field-Effect Transistors. *Science* **1996**, *272*, 1462–1464. [CrossRef]
98. Marcus, R.A. On the Theory of Oxidation-Reduction Reactions Involving Electron Transfer. II. Applications to Data on the Rates of Isotopic Exchange Reactions. *J. Chem. Phys.* **1957**, *26*, 867–871. [CrossRef]
99. Cao, R.; Cheng, Y.; Wang, R.; Wen, J.; Zhu, L.; Kong, W.; Qiao, X.; Zhu, M. Polymer-based hybrid materials and their application in personal health. *Nano Res.* **2022**, *16*, 3956–3975. [CrossRef]
100. Zhao, Q.; Yu, X.; Xie, Z.; Liu, J.; Han, Y. Optimizing H-/J-Type Aggregation and Vertical Phase Separation To Improve Photovoltaic Efficiency of Small Molecule Solar Cells by Adding a Macromolecule Additive. *ACS Appl. Energy Mater.* **2018**, *1*, 6338–6344. [CrossRef]
101. Xie, R.; Weisen, A.R.; Lee, Y.; Aplan, M.A.; Fenton, A.M.; Masucci, A.E.; Kempe, F.; Sommer, M.; Pester, C.W.; Colby, R.H.; et al. Glass transition temperature from the chemical structure of conjugated polymers. *Nat. Commun.* **2020**, *11*, 893. [CrossRef]
102. Kurosawa, T.; Gu, X.; Gu, K.L.; Zhou, Y.; Yan, H.; Wang, C.; Wang, G.J.N.; Toney, M.F.; Bao, Z. Understanding the Impact of Oligomeric Polystyrene Side Chain Arrangement on the All-Polymer Solar Cell Performance. *Adv. Energy Mater.* **2017**, *8*, 1701552. [CrossRef]
103. Liu, J.; Yin, Y.; Wang, K.; Wei, P.; Lu, H.; Song, C.; Liang, Q.; Huang, W. Domain size control in all-polymer solar cells. *iScience* **2022**, *25*, 104090. [CrossRef]
104. Liu, J.; Zeng, S.; Zhang, Z.; Peng, J.; Liang, Q. Optimizing the Phase-Separated Domain Size of the Active Layer via Sequential Crystallization in All-Polymer Solar Cells. *J. Chem. Phys. Lett.* **2020**, *11*, 2314–2321. [CrossRef]
105. Ye, L.; Xiong, Y.; Chen, Z.; Zhang, Q.; Fei, Z.; Henry, R.; Heeney, M.; O'Connor, B.T.; You, W.; Ade, H. Sequential Deposition of Organic Films with Eco-Compatible Solvents Improves Performance and Enables Over 12%-Efficiency Nonfullerene Solar Cells. *Adv. Mater.* **2019**, *31*, e1808153. [CrossRef]
106. Li, Z.; Xu, X.; Zhang, W.; Meng, X.; Ma, W.; Yartsev, A.; Inganas, O.; Andersson, M.R.; Janssen, R.A.; Wang, E. High Performance All-Polymer Solar Cells by Synergistic Effects of Fine-Tuned Crystallinity and Solvent Annealing. *J. Am. Chem. Soc.* **2016**, *138*, 10935–10944. [CrossRef]
107. Nilsson, S.; Bernasik, A.; Budkowski, A.; Moons, E. Morphology and phase segregation of spin-casted films of Polyfluorene/PCBM blends. *Macromolecules* **2007**, *40*, 8291–8301. [CrossRef]
108. Hou, J.; Inganas, O.; Friend, R.H.; Gao, F. Organic solar cells based on non-fullerene acceptors. *Nat. Mater.* **2018**, *17*, 119–128. [CrossRef]
109. Zhou, K.; Liu, Y.; Alotaibi, A.; Yuan, J.; Jiang, C.; Xin, J.; Liu, X.; Collins, B.A.; Zhang, F.; Ma, W. Molecular and Energetic Order Dominate the Photocurrent Generation Process in Organic Solar Cells with Small Energetic Offsets. *ACS Energy Lett.* **2020**, *5*, 589–596. [CrossRef]
110. Perdigon-Toro, L.; Zhang, H.; Markina, A.; Yuan, J.; Hosseini, S.M.; Wolff, C.M.; Zuo, G.; Stolterfoht, M.; Zou, Y.; Gao, F.; et al. Barrierless Free Charge Generation in the High-Performance PM6:Y6 Bulk Heterojunction Non-Fullerene Solar Cell. *Adv. Mater.* **2020**, *32*, e1906763. [CrossRef]
111. Yao, H.; Cui, Y.; Qian, D.; Ponseca, C.S., Jr.; Honarfar, A.; Xu, Y.; Xin, J.; Chen, Z.; Hong, L.; Gao, B.; et al. 14.7% Efficiency Organic Photovoltaic Cells Enabled by Active Materials with a Large Electrostatic Potential Difference. *J. Am. Chem. Soc.* **2019**, *141*, 7743–7750. [CrossRef] [PubMed]

112. Dong, Y.; Zou, Y.; Yuan, J.; Yang, H.; Wu, Y.; Cui, C.; Li, Y. Ternary Polymer Solar Cells Facilitating Improved Efficiency and Stability. *Adv. Mater.* **2019**, *31*, e1904601. [CrossRef] [PubMed]
113. Liu, J.; Lu, H.; Yin, Y.; Wang, K.; Wei, P.; Song, C.; Miao, Z.; Liang, Q. Thermodynamic and kinetic insights for regulating molecular orientation in nonfullerene all-small-molecule solar cells. *Battery Energy* **2022**, *1*, 20220013. [CrossRef]
114. An, Y.K.; Liao, X.F.; Chen, L.; Xie, Q.; Zhang, M.; Huang, B.; Liao, Z.H.; Guo, H.; Jazib, A.; Han, J.H.; et al. A_1–A_2 Type Wide Bandgap Polymers for High-Performance Polymer Solar Cells: Energy Loss and Morphology. *Solar RRL* **2019**, *3*, 1800291. [CrossRef]
115. Nam, M.; Kang, J.h.; Shin, J.; Na, J.; Park, Y.; Cho, J.; Kim, B.; Lee, H.H.; Chang, R.; Ko, D.H. Ternary Organic Blend Approaches for High Photovoltaic Performance in Versatile Applications. *Adv. Energy Mater.* **2019**, *9*, 1901856. [CrossRef]
116. Güldal, N.S.; Kassar, T.; Berlinghof, M.; Ameri, T.; Osvet, A.; Pacios, R.; Li Destri, G.; Unruh, T.; Brabec, C.J. Real-time evaluation of thin film drying kinetics using an advanced, multi-probe optical setup. *J. Mater. Chem. C* **2016**, *4*, 2178–2186. [CrossRef]

Disclaimer/Publisher's Note: The statements, opinions and data contained in all publications are solely those of the individual author(s) and contributor(s) and not of MDPI and/or the editor(s). MDPI and/or the editor(s) disclaim responsibility for any injury to people or property resulting from any ideas, methods, instructions or products referred to in the content.